



Elastic constants determination of anisotropic materials by depth-sensing indentation

Caterina Lamuta¹

© Springer Nature Switzerland AG 2019

Abstract

Depth-sensing indentation is a useful and powerful tool for the mechanical characterization of materials at the micro and nano scale. This technique allows the determination of the Young modulus from the analysis of the load-penetration depth curve according to specific theoretical models. One of the most used models is that one proposed by Oliver and Pharr. However, when a material with anisotropic mechanical properties is tested, Oliver and Pharr's theory is no longer suitable to describe the contact mechanics between the indenter tip and the tested material. This paper provides an overview of the theoretical models developed for the evaluation of the elastic constants of anisotropic materials through depth-sensing indentation. Specifically, the cases of generally anisotropic and orthotropic materials are described in order to cover the entire range of anisotropy. Examples on how these models can be applied for the mechanical characterization of generally anisotropic topological insulators and transversely isotropic pyrolytic carbon are also reported. This topical overview represents a useful tutorial for the evaluation of the elastic constants of anisotropic materials by depth-sensing indentation by shading light on the contact mechanics at the micro and nano scale.

Keywords Depth-sensing indentation · Indentation modulus · Elastic mechanical properties · Anisotropic materials · Density functional theory · Topological insulators · Pyrolytic carbon

1 Introduction

Indentation experiments have been extensively used since 1822 to measure the hardness of materials [1]. The introduction of depth-sensing indentation allowed to measure also the elastic properties of solids (i.e., Young's modulus) through the real-time monitoring of the applied indentation load and the penetration depth of the indenter tip [2]. Very small volumes of materials, in the sub-micron range, can be tested with depth-sensing indentation, which is one of the most powerful experimental tools for the mechanical characterization of thin films, coatings, nanocomposites, and heterogeneous structures. In a typical depth-sensing indentation tests, an indenter tip is driven into the tested material until a target load or penetration depth is reached. This process is usually performed at constant loading or constant displacement rate. After a

short hold period at maximum indentation load, the tip is gradually retracted from the material surface. Tabor [3] and Stilwell and Tabor [4] observed that the elastic modulus of the tested material is related to the displacement recovered during the unloading process and can be calculated from the theory of elasticity. Doerner and Nix [5] modelled the unloading process as a contact problem of a rigid punch on an elastically half space. Using these assumptions, Pharr et al. [6] demonstrated that the indentation modulus M of a tested material is related to the slope of the unloading curve S (i.e., the contact stiffness) through the following relationships:

$$S = \frac{dP}{dh} = \frac{2}{\sqrt{\pi}} M \sqrt{A} \quad (1)$$

✉ Caterina Lamuta, caterina-lamuta@uiowa.edu | ¹Department of Mechanical Engineering, University of Iowa, Iowa City, IA 52242, USA.



where P is the indentation load, h the penetration depth (i.e., the rigid-body displacement of the indenter relative to the half-space), and A the projected contact area. The indentation modulus M , also called reduced Young modulus E_r , depends on the elastic properties of the tested material, according to the following equation [6]:

$$\frac{1}{M} = \frac{1}{E_r} = \frac{1 - \nu^2}{E} + \frac{1 - \nu_i^2}{E_i} \quad (2)$$

where E and ν are the Young modulus and the Poisson ratio of the tested material while E_i and ν_i are the Young modulus and the Poisson ratio of the indenter material (usually $E_i = 1141$ GPa and $\nu_i = 0.07$ for a diamond tip). After S is experimentally measured from the unloading curve, the Young modulus E of a tested material, can then be calculated using Eqs. (1, 2), if the value of the projected contact area A is known. The projected contact area can be obtained from the indenter penetration depth through simple geometrical relationships, such as Eqs. (3, 4), which refer to indenter tips with a spherical and conical geometry, respectively:

$$A = 2\pi R h_c \quad (3)$$

$$A = \pi h_c^2 \tan^2(\alpha). \quad (4)$$

R is the radius of the spherical indenter, α the cone half-angle, and h_c is the effective penetration depth. However, during an indentation test, only the maximum penetration depth h_{\max} can be experimentally measured by means of displacement sensors and such value differs from the real penetration depth h_c due to the deflection of the surface of tested sample (a downward deflection is known as “sink-in” while an upward deformation is known as pile-up phenomenon) Oliver and Pharr [7] proposed the following equation for the calculation of the real penetration depth, h_c :

$$h_c = h_{\max} - \varepsilon \frac{P_{\max}}{S} \quad (5)$$

where ε is the intercept factor, equal to $\frac{3}{4}$.

The measurement of the elastic stiffness through Eqs. (1–5) refers to isotropic materials, characterized by the same mechanical properties in all directions. When anisotropic materials (i.e., materials with different properties along different directions) are tested by depth-sensing indentation, Eq. (2) is no longer suitable to describe the relationship between the indentation modulus M and the elastic constants of such materials. Different theoretical models have been developed to obtain the equivalent of Eq. (2) for anisotropic materials. After a brief introduction on the stress/strain relationship of anisotropic materials, two of the most used models, referred to generally

anisotropic and orthotropic materials respectively, will be described in this paper. An implementation of these models for the mechanical characterization of generally anisotropic topological insulators and transversely isotropic pyrolytic carbon will be finally described.

2 Hooke's law for anisotropic materials

The stress/strain relationship (i.e., the Hooke's law) of generally anisotropic materials with linear elastic behavior can be written as follows:

$$\sigma_{ij} = C_{ijkl} \varepsilon_{kl} \quad (6)$$

where σ_{ij} are the stress components, ε_{ij} the strain components, and C_{ijkl} the elastic moduli. Considering the following symmetry properties [8, 9]:

$$\sigma_{ij} = \sigma_{ji} \quad (7)$$

$$\varepsilon_{kl} = \varepsilon_{lk} \quad (8)$$

$$C_{ijkl} = C_{jikl}, \quad C_{ijkl} = C_{ijlk}, \quad C_{ijkl} = C_{klij} \quad (9)$$

the generalized Hooke's law can be written in matrix form as:

$$\begin{pmatrix} \sigma_{11} \\ \sigma_{22} \\ \sigma_{33} \\ \sigma_{23} \\ \sigma_{13} \\ \sigma_{12} \end{pmatrix} = \begin{bmatrix} C_{11} & C_{12} & C_{13} & C_{14} & C_{15} & C_{16} \\ C_{12} & C_{22} & C_{23} & C_{24} & C_{25} & C_{26} \\ C_{13} & C_{23} & C_{33} & C_{34} & C_{35} & C_{36} \\ C_{14} & C_{24} & C_{34} & C_{44} & C_{45} & C_{46} \\ C_{15} & C_{25} & C_{35} & C_{45} & C_{55} & C_{56} \\ C_{16} & C_{26} & C_{36} & C_{46} & C_{56} & C_{66} \end{bmatrix} \begin{pmatrix} \varepsilon_{11} \\ \varepsilon_{22} \\ \varepsilon_{33} \\ 2\varepsilon_{23} \\ 2\varepsilon_{13} \\ 2\varepsilon_{12} \end{pmatrix}. \quad (10)$$

The generic stiffness constant C_{mn} in the matrix of Eq. (10), is equal to the elastic modulus C_{ijkl} , where $m = i$ if $i = j$ or $m = 9 - i - j$ if $i \neq j$, and $n = k$ if $k = l$ or $n = 9 - k - l$ if $k \neq l$. Due to symmetry properties of Eq. (9), $C_{mn} = C_{nm}$ and the matrix in Eq. (10) is symmetric. The stiffness constants C_{mn} can be expressed as function of the material elastic constants, i.e., Young modulus E_{mn} , Poisson ratio ν_{mn} , and shear modulus G_{mn} . A generally anisotropic material is characterized by 21 independent elastic constants. An anisotropic material is defined orthotropic when shows properties that differ along three mutually-orthogonal twofold axes of rotational symmetry. For orthotropic materials, only 9 elastic constants in the matrix of Eq. (10) are independent. Isotropic materials have only 2 independent elastic constants, i.e., the Young modulus E and the Poisson ratio ν [the shear modulus G can be calculated as $G = E/2(1 + \nu)$]. It is then clear how Eq. (2) is suitable only for isotropic materials, since relates the indentation modulus M only to one value of Young modulus and Poisson ratio.

3 Indentation modulus for generally anisotropic materials

The relationship between the contact stiffness S and the indentation modulus M of Eq. (1), derived from the fundamental Hertz contact solution [10], is valid for generally anisotropic materials and it does not depend on the indenter geometry. However, the relationship between the indentation modulus and the material elastic constants expressed in Eq. (2) applies only to elastically isotropic materials (M in this case reduces to the plane-strain elastic modulus). Due to the large number of independent elastic constants of generally anisotropic materials (i.e., 21), the relationship between the indentation modulus and the elastic constants becomes far more complicated than that one reported in Eq. (2). A few mathematical formulations have been proposed to model the Hertzian contact between the indenter tip and anisotropic materials and estimate the relationship between the indentation modulus and the material elastic constants. The theoretical model developed by Vlassak et al. [11] can be considered the most general and refined solution, valid for materials with any degree of anisotropy and indenters of arbitrary shape. The model is described below and represents a powerful tool for the mechanical characterization of anisotropic materials by depth-sensing indentation.

In the theoretical formulation by Vlassak et al., a general anisotropic elastic material is modeled as a general anisotropic elastic half-space, as shown in Fig. 1. A Cartesian coordinate system (y_1, y_2, y_3) has its origin in the boundary of the half-space, which is arbitrarily oriented with respect to the coordinate axes y_1, y_2, y_3 . The orientation of the boundary of the half-space is given by the direction cosines of the outer normal to the boundary, $(\alpha_1, \alpha_2, \alpha_3)$, in red in Fig. 1. Let's define t as a unit vector lying in the half-space boundary, and m and n as orthogonal unit vectors lying in the plane perpendicular to t (light blue plane in Fig. 1) so that (m, n, t) represent a triad of right-hand

vectors (yellow in Fig. 1). The orientation of the m and n vectors is given by the angle φ between m and the normal to the half-space surface.

Using the Stroh formalism, the Barnett and Lothe matrix $B(t)$ is defined as follows [12]:

$$B_{js}(t) = B_{sj}(t) = \frac{1}{8\pi^2} \int_0^{2\pi} \{ (mm)_{js} - (mn)_{jk} (nn)_{kr}^{-1} (nm)_{rs} \} d\varphi \tag{11}$$

where for any generic vector a and b , each generic matrix (ab) in the integral is defined by:

$$(ab)_{jk} = a_i C_{ijkm} b_m \tag{12}$$

and C_{ijkl} are the elastic stiffnesses of the generally anisotropic material in the Cartesian coordinate system (y_1, y_2, y_3) . In Eq. (12) repeated indices imply a summation over the repeated index from 1 to 3.

An indentation test is now modeled by considering a concentrated unit force applied in the origin of the coordinate system (y_1, y_2, y_3) , perpendicular to the boundary of the half-space surface (along the direction $(-\alpha_1, -\alpha_2, -\alpha_3)$ defined by the unit vector of the inner normal). Vlassak et al. [11] demonstrated that the normal displacement $w(y)$ of a generic point Q of the half-space surface, in the direction of the applied load, is given by:

$$w(y) = \frac{1}{8\pi^2 |y|} \left[\alpha_k B_{km}^{-1} \left(\frac{y}{|y|} \alpha_m \right) \right] = \frac{h(\theta)}{r} \tag{13}$$

where y is the position vector of Q , and $r = |y| = \sqrt{y_1^2 + y_2^2 + y_3^2}$, while θ is the angle between the position vector y (green in Fig. 1) and some fixed datum in the half-space surface. If we take this datum to be x_1 -axis (purple in Fig. 1), we can consider the position of Q in polar coordinates in the half-space surface, so that $x_1 = r \cos(\theta)$, and $x_2 = r \sin(\theta)$. $h(\theta)$ can be calculated from Eq. (13) by solving the integral of Eq. (11) to obtain B_{km}^{-1} . For generally anisotropic materials a closed-form solution of Eq. (11) does not exist and the integral has to be solved by numerical integration. One of the most used approaches to solve Eq. (13) is to develop $h(\theta)$ as a Fourier series in terms of the angle 2θ [13], as follows:

$$h(\theta) = h_0 + \sum_{n=1}^{\infty} h_{cn} \cos 2n\theta + h_{sn} \sin 2n\theta \tag{14}$$

where the Fourier coefficients are:

$$h_0 = \frac{1}{2\pi} \int_0^{2\pi} h(\theta) d\theta, \quad \left\{ \begin{matrix} h_{cn} \\ h_{sn} \end{matrix} \right\} = \frac{1}{\pi} \int_0^{2\pi} h(\theta) \left\{ \begin{matrix} \cos 2n\theta \\ \sin 2n\theta \end{matrix} \right\} d\theta. \tag{15}$$

Considering the mathematical formulation of Eq. (13) for the indentation penetration depth, and the relationship

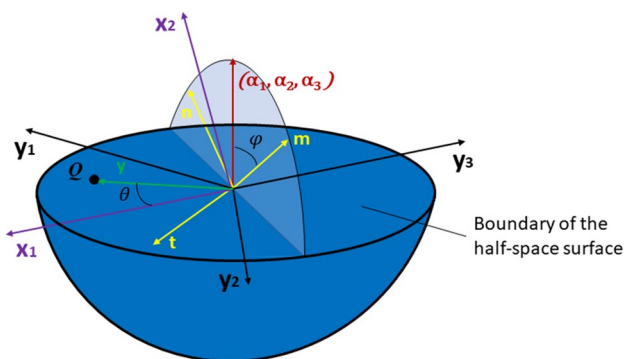


Fig. 1 Schematic representation of the half-space

in Eq. (1), Vlassak et al. [11] obtained the estimation of the indentation modulus for generally anisotropic materials considering two different approximations: elliptical and circular contact area, respectively. When the contact area between the indenter and the half-space is assumed to be elliptical, the equivalent indentation modulus of the half-space (i.e., the generally anisotropic material) is given by:

$$M_{eqv} = \frac{1}{\alpha(e, \varphi)(1 - e^2)^{1/4}} \quad (16)$$

where $e = \sqrt{1 - (b^2 - a^2)}$ is the eccentricity of the ellipse (with a semimajor and b semiminor axes), and $\alpha(e, \varphi)$ is given by the following equation:

$$\alpha(e, \varphi) = \int_0^\pi \frac{h(\theta + \varphi)}{\sqrt{1 - e^2 \cos \theta}} d\theta. \quad (17)$$

It is worth noting that the elastic constants of the anisotropic materials are contained in the h term, calculated by Eqs. (11–13).

When the contact area is assumed to be circular, the equivalent indentation modulus is given by:

$$M_{eqv} = \frac{1}{\pi h_0} \quad (18)$$

where h_0 is the first-order term of the Fourier series representation of the function $h(\theta)$, which does not depend on the angle θ .

When an axisymmetric indenter is used, and the contact area is circular (i.e., perfect axisymmetric contact case), M_{eqv} in Eq. (18) represents the exact equivalent of M in Eq. (2) for generally anisotropic materials. In this case the indentation modulus does not depend on the indentation angle θ . In the general case of non-axisymmetric contact problem, only approximate solutions can be provided by the model of Vlassak et al. In particular, two different types of approximations can be considered. First, the contact area can be assumed to be circular, and Eq. (18) can be used to estimate the equivalent indentation modulus; second, the contact area can be assumed to be elliptical and Eq. (16) can be used to estimate the equivalent indentation modulus for generally anisotropic

materials. For indenters with elongated geometry, the second approximation is usually more accurate. Vlassak et al. [11] experimentally validated their model by testing different anisotropic materials and a good agreement between theoretical and experimental predictions was found for both axisymmetric and non-axisymmetric indenters.

4 Indentation modulus for orthotropic materials

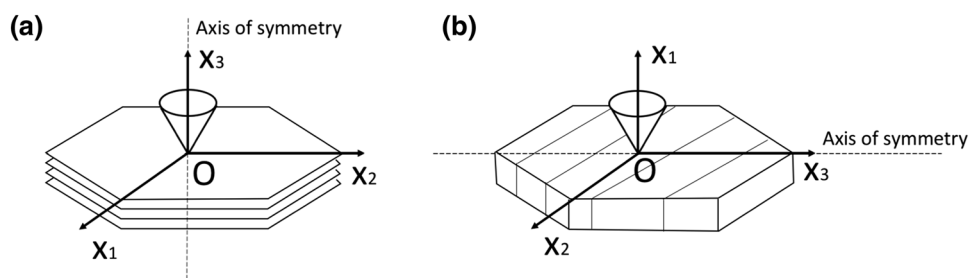
For generally anisotropic materials a closed-form solution for the estimation of the indentation modulus from the elastic constants of the material does not exist. As discussed in the previous section, numerical integration is needed to calculate the function $h(\theta)$ from Eqs. (11–13) and estimate M_{eqv} from Eq. (16) or Eq. (18). The mathematical formulation is instead less complex for orthotropic materials, for which an explicit solution for $h(\theta)$ can be obtained. Dalafargue and Ulm [14] considered the generic formulation of Vlassak et al. [11] and derived a theoretical model for the calculation of the indentation modulus of general elastically orthotropic and transversely isotropic materials, considering conical indenters. This section describes this model by providing the equations useful for its implementation.

4.1 Transversely isotropic materials

Transversely isotropic materials are a sub-group of orthotropic materials. An orthotropic material is defined transversely isotropic when its mechanical properties are symmetric about an axis that is normal to a plane of isotropy (in the latter the material properties are the same in all directions). Transversely isotropic materials are characterized by five independent elastic constants. Specifically, these independent constants are C_{11} , C_{33} , C_{44} , C_{13} , C_{12} if the reference system of Fig. 2a is considered, where x_3 is the axis of symmetry.

Let's assume to indent a transversely isotropic material with a conical indenter along the axis of symmetry, as shown in Fig. 2a.

Fig. 2 Indentation of a transversely isotropic material by conical indenter tip. **a** Along the axis of symmetry, **b** orthogonal to the axis of symmetry



In this configuration the half-space surface is parallel to the plane of isotropy (x_1, x_2) . Since the indenter is axisymmetric and the indentation is performed along the axis of symmetry, this test corresponds to a perfect axisymmetric contact case, where the contact area is circular. Equation (18) can then be used to calculate the indentation modulus M_3 along this indentation direction:

$$M_3 = \frac{1}{\pi H} \tag{19}$$

where H is the constant of the Green's function of Eq. (13), which can be directly calculated from the elastic constants of transversely isotropic materials, as follows, without recurring to numerical integration [14]:

$$H = \frac{1}{2\pi} \sqrt{\frac{C_{11}}{C_{31}^2 - C_{13}^2} \left(\frac{1}{C_{44}} + \frac{2}{C_{31} + C_{13}} \right)}. \tag{20}$$

If the indentation is performed perpendicularly to the axis of symmetry, as shown in Fig. 2b, the perfect axisymmetric contact case no longer applies because, although the conical indenter is axisymmetric, the contact area cannot be considered circular in the (x_2, x_3) plane (i.e., the material deforms differently along x_2 - and x_3 -axes). In this case the approximation of the elliptical contact area proposed by Vlassak et al. [11] can be considered, and the indentation modulus can be calculated by means of Eq. (16). The function $h(\theta)$ is calculated from Eqs. (11–15). However, due to symmetry properties of the transversely isotropic material, no numerical integration is needed, and an explicit equation for $h(\theta)$ is obtained using a first order approximation of the Fourier series:

$$h(\theta) = h_0 + h_{c1} \cos 2\theta \tag{21}$$

where

$$h_0 = \frac{H_2 + H_3}{2}, \quad h_{c1} = \frac{H_2 - H_3}{2} \tag{22}$$

$$H_2 = \frac{1}{2\pi} \sqrt{\frac{C_{33}}{C_{31}^2 - C_{13}^2} \left(\frac{1}{C_{44}} + \frac{2}{C_{31} - C_{13}} \right)} \tag{23}$$

$$H_3 = \frac{1}{\pi} \frac{C_{11}}{C_{11}^2 - C_{12}^2}. \tag{24}$$

By using Eqs. (21–24) into Eqs. (16, 17) (for additional computational details, we kindly invite the reader to refer to [14]), the indentation modulus M_1 in the direction perpendicular to the axis of symmetry, is calculated as follows:

$$M_1 = \frac{1}{\pi \sqrt{H_2 H_3}} = \sqrt{M_{12} M_{13}} \tag{25}$$

where M_{13} is the indentation modulus considering an isotropic solid (with same properties along directions x_1, x_2, x_3), and M_{12} the indentation modulus in direction x_1 by setting the same mechanical properties for directions x_2 and x_3 :

$$M_{13} = \frac{1}{\pi H_3} = \frac{C_{11}^2 - C_{12}^2}{C_{11}} \tag{26}$$

$$M_{12} = \frac{1}{\pi H_2} = \sqrt{\frac{C_{11}}{C_{33}}} M_3. \tag{27}$$

4.2 Generally orthotropic materials

A generally orthotropic material is characterized by 9 independent elastic constants: $C_{11}, C_{22}, C_{33}, C_{44}, C_{55}, C_{66}, C_{12}, C_{13}, C_{23}$. If we consider a Cartesian coordinate system (x_1, x_2, x_3) , with 3 planes of symmetry $(x_1, x_2), (x_1, x_3), (x_2, x_3)$, the indentation moduli along x_1, x_2 , and x_3 can be obtained by following the same procedure of Sect. 4.1 [14]:

$$M_1 = \sqrt{M_{12} M_{13}} \tag{28}$$

$$M_2 = \sqrt{M_{21} M_{23}} \tag{29}$$

$$M_3 = \sqrt{M_{31} M_{32}} \tag{30}$$

where

$$M_{21} = 2 \sqrt{\frac{C_{21}^2 - C_{12}^2}{C_{11}} \left(\frac{1}{C_{66}} + \frac{2}{C_{21} + C_{12}} \right)^{-1}} \tag{31}$$

$$M_{31} = 2 \sqrt{\frac{C_{31}^2 - C_{13}^2}{C_{11}} \left(\frac{1}{C_{55}} + \frac{2}{C_{31} + C_{13}} \right)^{-1}} \tag{32}$$

$$M_{32} = 2 \sqrt{\frac{C_{32}^2 - C_{23}^2}{C_{22}} \left(\frac{1}{C_{44}} + \frac{2}{C_{32} + C_{23}} \right)^{-1}} \tag{33}$$

$$M_{12} = M_{21} \sqrt{\frac{C_{11}}{C_{22}}} \tag{34}$$

$$M_{13} = M_{31} \sqrt{\frac{C_{11}}{C_{33}}} \tag{35}$$

$$M_{23} = M_{32} \sqrt{\frac{C_{22}}{C_{33}}}. \tag{36}$$

5 Indentation modulus of generally anisotropic topological insulators

In this section we describe how depth-sensing indentation and the theoretical model by Vlassak et al. [11] (described in Sect. 3) were used to validate computational results from density functional theory (DFT) on the evaluation of the elastic constants of the topological insulator Bi_2Te_3 . Further details about the results discussed herein can be found in the work from Lamuta et al. [15].

3D topological insulators are considered a novel topological phase of matter, and are gaining growing interest from the worldwide scientific community [16–18], due to their promising applications in optoelectronics [19], plasmonics [20], spintronics [21], quantum computing [22], and thermoelectric devices [17, 23, 24]. Bi_2Te_3 and Bi_2Se_3 represent the most studied topological insulators, due to their large energy gap (~ 0.2 – 0.3 eV) that allows applications at room temperature [15, 25–29]. In this section we focus on Bi_2Te_3 , a layered and anisotropic material, whose atomic structure is illustrated in Fig. 3. Bi_2Te_3 is characterized by quintuple layers (QLs). Adjacent QLs are separated by weak Van der Waals bonds and are internally characterized by strong covalent bonds [27]. Due to this specific crystal structure, Bi_2Te_3 belongs to the D_{3d}^5 (R-3 m) space group and is characterized by 6 independent elastic constants, namely C_{11} , C_{12} , C_{13} , C_{14} , C_{33} , C_{44} .

Lamuta et al. [15] calculated the elastic properties of Bi_2Te_3 by means of DFT simulations. A rhombohedral unit cell was used to simulate the topological insulator (shown in Fig. 3). The 6 independent elastic constants of Bi_2Te_3 were calculated using DFT, as implemented in the QUANTUM-ESPRESSO package [30], using a norm conserving scalar relativistic pseudopotentials with only the outermost s and p states in valence band. Two different approximations were used for the exchange–correlation energy functional, namely the local density approximation (LDA) [31], and the generalized gradient Perdew–Burke–Ernzerhof (PBE) approximation [32]. A semiempirical Van der Waals correction was added to the PBE approximation, as described in [33]. The electronic wave functions were expanded in plane waves up to a 90 Ry energy cut-off. A non-elemental hexagonal cell (shown in Fig. 3) and an integration of the Brillouin zone over a $8 \times 8 \times 2$ Monkhorst–Pack mesh [34] were used to optimize the bulk geometry. A force threshold value of 5×10^{-5} a.u. was used for the relaxation of the atomic positions.

Deformations from 0.2 to 2% were applied in order to calculate the elastic coefficients C_{mn} from the stress/strain profile, according to the procedure described in [35, 36]. In Table 1, the six independent coefficients of the stiffness matrix of Bi_2Te_3 , obtained with both the LDA approximation and the PBE approximation with the semiempirical Van der Waals correction (PBE+VDW), are reported.

To validate DFT results of Table 1 and understand which one between LDA and PBE+VDW approximations is the most suitable for Bi_2Te_3 , Lamuta et al. used depth-sensing

Fig. 3 Crystal structure of Bi_2Te_3 . On the right, rhombohedral unit cell and hexagonal conventional cell (bismuth atoms are represented in red, tellurium atoms in blue)

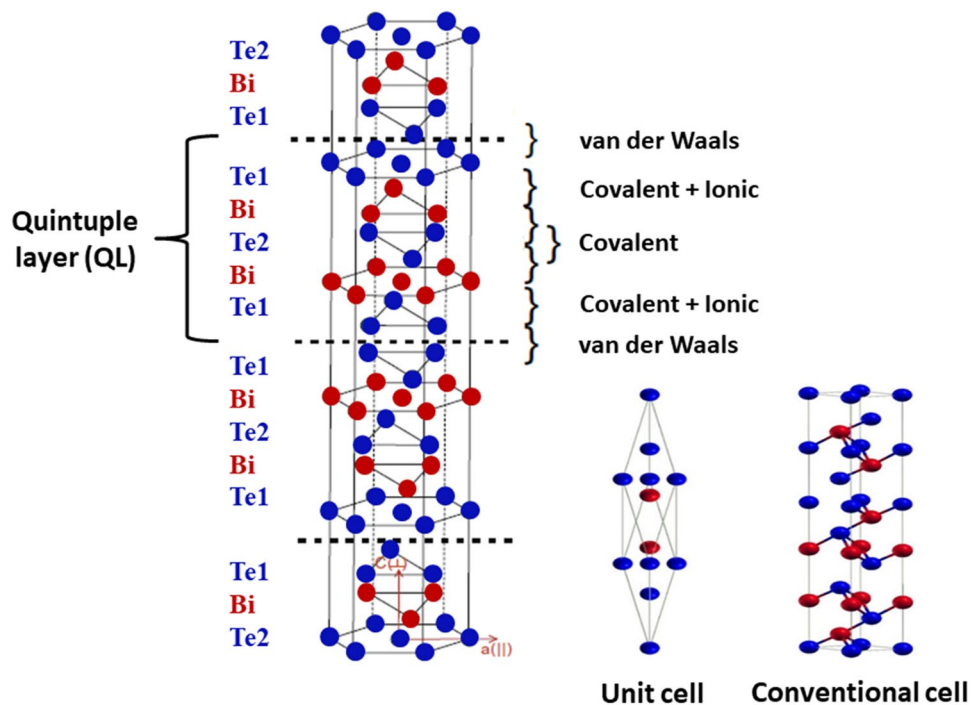


Table 1 Independent elastic coefficients C_{mn} of Bi_2Te_3 calculated by DFT simulations using LDA and PBE + VDW approximations [15]

	C_{11}	C_{12}	C_{13}	C_{14}	C_{33}	C_{44}
LDA	81.5	22.2	31.2	19.4	56.4	42.7
PBE – VDW	78.3	13.8	23.2	20.7	35.7	35.5

Table 2 Theoretical indentation moduli M_T calculated using the elastic constants of Table 1 and Eqs. (11–15, 18) in the direction parallel and perpendicular to the material lamellae [15]

	M_t perpendicular to the lamellae (GPa)	M_t parallel to the lamellae (GPa)
LDA	60.21	69.45
PBE – VDW	42.46	62.40

indentation combined with the theoretical model from Vlassak et al. [11].

Since Bi_2Te_3 belongs to the D_{3d}^5 (R-3 m) space group and it cannot be considered an orthotropic material, the model proposed by Vlassak et al. for generally anisotropic materials, described in Sect. 3, was used to calculate the theoretical indentation modulus M_T , using the 6 independent elastic constants calculated by DFT. Since Bi_2Te_3 does not present any isotropy plane, the condition of perfect axisymmetric contact is never guaranteed, and only approximate solutions can be found for the indentation modulus, according to the Vlassak et al. model [11].

Lamuta et al. [15], considered the approximation of a circular contact area, and used Eq. (18) to calculate the indentation modulus along 2 different directions, parallel and perpendicular to the material lamellae (i.e., each lamella corresponds to a quintuple layer (QL), and lies in the Bi_2Te_3 basal plane), respectively. Equations (11–15) were used to calculate h_0 [the first-order term of the Fourier series representation of the function $h(\theta)$] through numerical integration. Results are reported in Table 2.

To experimentally validate DFT results of Table 1, depth-sensing indentation tests were performed to compare the experimental indentation modulus M_E to the theoretical modulus M_T (calculated using the DFT elastic constants of Table 1 and the theoretical model by Vlassak et al.). A spherical indenter tip ($R = 20 \mu\text{m}$, $\alpha = 90^\circ$) was used and indentations were performed in the directions perpendicular and parallel to Bi_2Te_3 lamellae. It is worth noting that the choice of an axisymmetric spherical indenter justifies the adopted approximation of a circular contact area (the elliptical contact area approximation is more suitable for indenters with elongated geometry).

Indentation tests were performed using the technique of the continuous stiffness measurements (CSM) [37], consisting in the application of a small oscillation to the

force signal during the indentation process. Thanks to this technique, the profile of the indentation modulus can be calculated dynamically for increasing values of penetration depth for each small loading/unloading cycle during one single indentation. Indentations parallel to the Bi_2Te_3 lamellae were performed using a maximum load of 5 mN, loading and unloading rate of 5 mN/min and 20 mN/min respectively, dwell time at maximum load of 10 s. The amplitude and the frequency of the sinusoidal force oscillation were set to 0.5 mN and 20 Hz, respectively. Indentations perpendicular to the Bi_2Te_3 lamellae were performed using the following parameters: maximum load 10 mN, loading and unloading rate of 10 mN/min and 40 mN/min respectively, dwell time at maximum load of 10 s. The amplitude and the frequency of the sinusoidal force oscillation were set to 1 mN and 20 Hz, respectively.

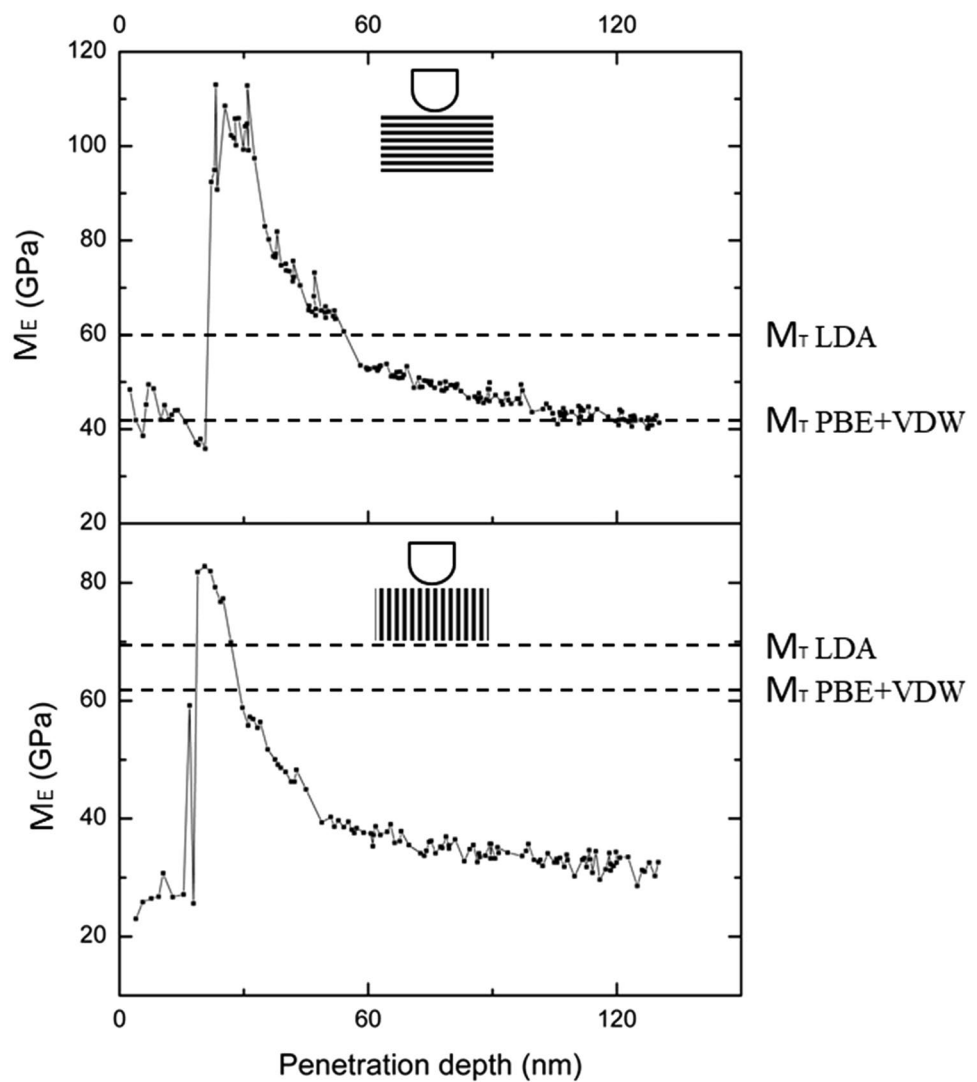
The experimental indentation modulus M_E was obtained according to the Oliver and Pharr theory for isotropic materials [6, 7] using Eqs. (1–3, 5). According to the Vlassak et al. model [11], M_{eqv} of an anisotropic material coincides with M of the equivalent isotropic material. This coincidence is exact for perfect axisymmetric contact and it is approximated (circular or elliptical contact area approximations can be used) when the contact is not perfectly axisymmetric. In our example, M_T represents M_{eqv} under the circular contact area approximation, and will coincide with M_E (i.e., M of the equivalent isotropic material, calculated from Oliver and Pharr's theory), if the elastic constants of Table 1 are estimated correctly from DFT. Depth-sensing indentation, combined with Vlassak et al.'s model [11], represents then a powerful tool to validate DFT results related to the mechanical characterization of anisotropic materials at small scale.

Figure 4 shows the trend of the experimental indentation modulus M_E as a function of the penetration depth for both the indentation directions, perpendicular (top panel) and parallel (bottom panel) to the Bi_2Te_3 lamellae.

For both the directions parallel and perpendicular to the Bi_2Te_3 lamellae, the experimental indentation modulus M_E stabilizes when the penetration depth reaches a value of 120 nm. The stabilization is obtained only when the condition of full plasticity contact is satisfied, as discussed in [28].

As shown in the top panel of Fig. 4, along the direction perpendicular to the Bi_2Te_3 lamellae, the theoretical indentation modulus M_T calculated using the PBE + VDW

Fig. 4 Experimental indentation modulus M_E profile with increasing values of penetration depth for a CSM nanoindentation performed along the direction perpendicular (top panel) and parallel (bottom panel) to the basal plane (i.e., Bi_2Te_3 lamellae). The dashed lines represent the theoretical indentation modulus M_T calculated according to Eq. (18) using the C_{mn} constants calculated by DFT with the LDA and PBE+VDW approximations [15]



approximation is in perfect agreement with the stabilized experimental modulus M_E , while the theoretical modulus predicted using the LDA approximation is considerably higher than the experimental value. This result demonstrates that the PBE+VDW approximation properly describes the exchange–correlation energy functional of Bi_2Te_3 by leading to a correct estimation of the elastic mechanical properties of the material. The higher indentation modulus obtained with the LDA approximation can be ascribed to an over-binding problem. The LDA approximation usually overestimates the binding energy and leads to shorter bond lengths with respect to the experimental values. This discrepancy becomes more relevant if the LDA approximation is used to model materials containing weak Van der Waals bonds, such as multilayered Bi_2Te_3 [15].

As shown in the bottom panel of Fig. 4, none of the approximations used in the DFT analysis is able to predict the stabilized experimental indentation modulus M_E along

the direction parallel to the Bi_2Te_3 lamellae. Such difference can be ascribed to the nanobuckling experienced by the lamellae during the indentation tests. As observed for other layered materials such as pyrolytic carbon [38, 39], thin layers, bonded by weak Van der Waals bonds, can easily experience instability when compressed along a direction parallel to their surface. This instability, known as nanobuckling, causes a rigid vertical displacement during the indentation process, which is not considered in the theoretical models that describe the interaction between the indenter tip and the analyzed material, including the model by Vlassak et al. used to calculate M_T in the example described herein.

Besides the implementation described above related to topological insulators, the theoretical model by Vlassak et al. has been used for the evaluation of the elastic constants of several anisotropic materials such as wood [40, 41], $\text{KSr}_2\text{Nb}_5\text{O}_{15}$ ceramics [42], $\beta\text{-Si}_3\text{N}_4$ ceramic crystals

[43], Ni–Mn–Ga ferromagnetic shape memory alloys [44], and beetle exocuticle [45].

6 Indentation modulus of transversely isotropic pyrolytic carbon

In the previous section an example on how the theoretical model proposed by Vlassak et al. [11] is used to characterize generally anisotropic materials, such as Bi_2Te_3 topological insulator, is proposed. This section focuses on the implementation of the Delafargue and Ulm model [14] for the elastic characterization of a transversely isotropic material, i.e., pyrolytic carbon.

Bulk pyrolytic carbon (PyroC) exhibits strong microstructural anisotropy, which is strongly related to the precursor gas and manufacturing conditions [46–50]. Specifically, bulk PyroC is a layered material, where each layer lies in the plane of isotropy, as shown in Fig. 2. For this reason, PyroC can be considered a transversely isotropic material.

Gross et al. [38] used the theoretical model proposed by Delafargue and Ulm [14] to estimate the indentation modulus along the direction perpendicular and parallel to the plane of isotropy of PyroC and compared theoretical predictions with experimental measurements. The reference system illustrated in Fig. 2 was used. Equations (19, 20) were used to calculate the theoretical indentation modulus M_3 along the axis of symmetry, while Eqs. (25–27) were implemented to calculate the indentation modulus M_1 in the direction orthogonal to the axis of symmetry (i.e., parallel to the plane of symmetry). The elastic constants C_{11} , C_{33} , C_{44} , C_{13} , C_{12} were experimentally obtained by means of ultrasonic phase spectroscopy [48] and strain gage methods [49]. Depth-sensing indentations were performed along the

direction perpendicular and parallel to the plane of isotropy to obtain experimental values of the indentation moduli M_3 and M_1 , respectively.

Indentations were performed using three different indenter tips: a cube corner indenter with a 200 nm radius of curvature, a Berkovich indenter with a 200 nm radius of curvature, and a cono-spherical indenter with a 3 μm radius of curvature. Figure 5 shows the load-penetration depth curves obtained along the direction perpendicular (left) and parallel (right) to the plane of isotropy.

It is worth noting that the deformation of PyroC during indentation is entirely elastic, since no residual penetration depth is measured at the end of the unloading process. Due to this elastic response, the Oliver and Pharr theory cannot be used to evaluate the experimental value of the indentation modulus. In other words, due to the absence of an actual imprint (due to the absence of plastic deformation), Eqs. (1–5) cannot be used because the area of the imprint A is equal to zero. For this reason, Gross et al. used the Sneddon solution [51, 52] to evaluate the experimental value of the indentation modulus. This solution models the relationship between the indentation load P and the penetration depth h for a conical and a spherical indenter as follows:

$$P(h) = \frac{E}{1-\nu^2} \frac{2 \tan(\alpha)}{\pi} h^2 \quad (\text{conical indenter}) \quad (37)$$

$$P(h) = \frac{4E}{3(1-\nu^2)} \sqrt{R} h^{3/2} \quad (\text{spherical indenter}) \quad (38)$$

where α is the cone half-angle and R is the radius of the spherical indenter.

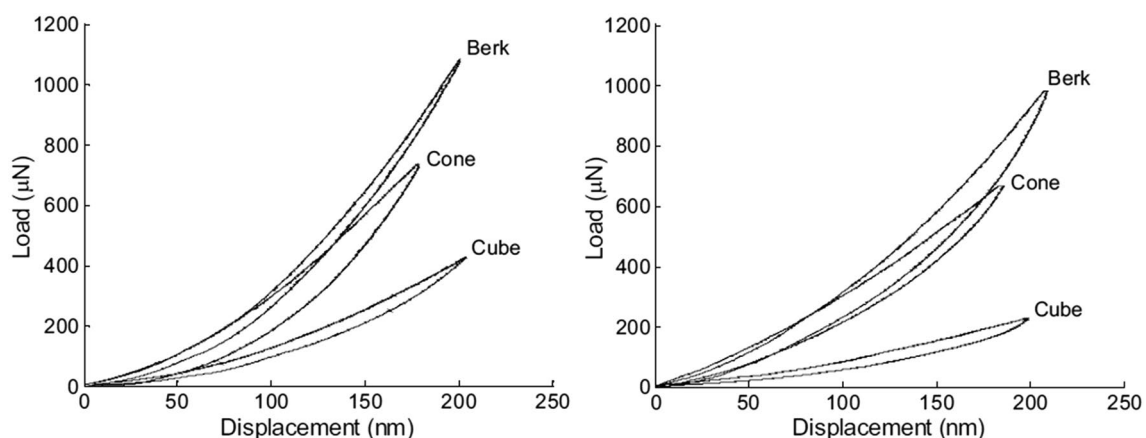


Fig. 5 Load-penetration depth curves for indentations normal to the plane of isotropy (left) and parallel to the plane of isotropy (right) of pyrolytic carbon. Different curves refer to different indenter tips [38]

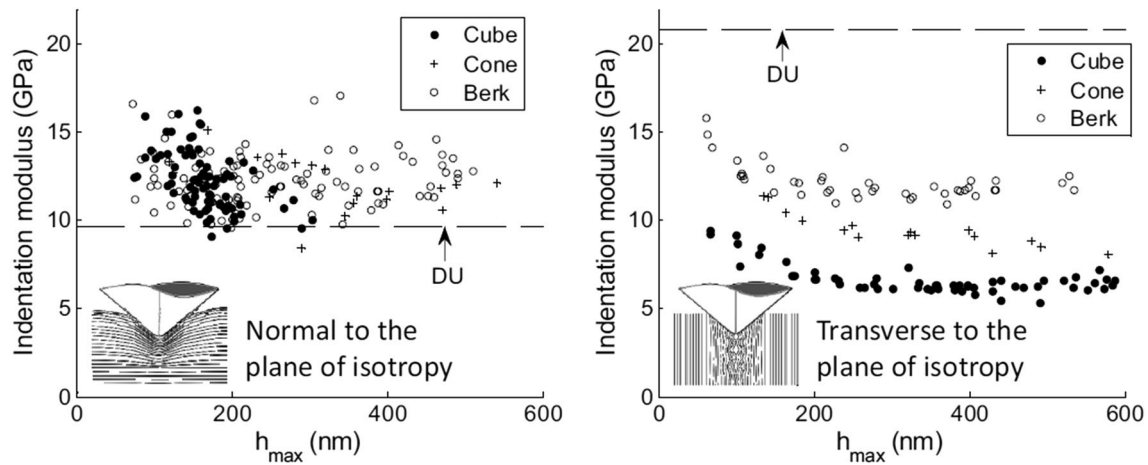


Fig. 6 Indentation modulus normal to the plane of isotropy (left plot) and parallel to the plane of isotropy (right plot). Theoretical values predicted from the Delafargue and Ulm model [14] are illustrated by the dashed line labeled DU [38]

Figure 6 shows the comparison between experimental and theoretical results.

As observed for topological insulators [15], the difference between theoretical and experimental results is larger in the direction parallel to the isotropy plane, due to nanobuckling [52, 53]. A better agreement is observed in the direction perpendicular to the plane of isotropy. However, a small discrepancy is still observed in this direction, as shown in the left of Fig. 6.

This discrepancy is due to the elastic deformation of PyroC. The theoretical model of Delafargue and Ulm considers an elasto-plastic deformation which involves the generation of a residual imprint on the materials surface. As previously discussed, PyroC experiences a fully elastic deformation during indentation, and this behavior is not modeled by Delafargue and Ulm.

Gross et al. [38] described also the influence of different indenter geometries on the nanobuckling generation, through finite element method (FEM) simulations. As shown in Fig. 7, when the indentation is performed along the plane of symmetry, the axial stress (in the direction of indentation) and the transverse tensile stress (perpendicular to the isotropy plane) exhibit higher values when a cube corner indenter is used. The combination between high axial stress and high transverse tensile stress fosters the nanobuckling phenomenon, by causing a decrement of the experimental value of the indentation modulus. This phenomenon explains why the lowest experimental indentation modulus is recorded in the direction parallel to the plane of isotropy when a cube corner indenter is considered (see right of Fig. 6).

The theoretical model of Delafargue and Ulm represents a powerful tool for the evaluation of the elastic constants

and indentation modulus of transversely isotropic materials at the nano and micro scale. Since it provides an explicit and exact solution, it can be easily implemented without requiring numerical integration or data fitting procedures. Besides the characterization of PyroC described in this section, this model has been used to characterize a wide variety of materials, including cortical bone [54], shale [55, 56], clay aggregates and minerals [57, 58], polycrystalline ZrB_2 ceramic [59], porous silica [60], sputtered ceramic thin films [61], AlN [62], and sol-gels [63].

7 Conclusion

This overview introduces the problem of the depth-sensing indentation of materials with anisotropic mechanical properties. Two different theoretical models for the evaluation of the indentation modulus of generally anisotropic (Vlassak et al.'s model) and orthotropic materials (Delafargue and Ulm's model), respectively, were described, and the equations useful for their implementation were provided. An example on how Vlassak et al.'s model can be used to experimentally validate density function theory (DFT) results on the elastic mechanical characterization of generally anisotropic materials at small scales is described. The example focuses on the characterization of the topological insulator Bi_2Te_3 , emerging anisotropic semiconductor with promising applications in optoelectronics. Depth-sensing indentation tests, combined with the theoretical model from Vlassak et al., showed that the generalized gradient Perdew–Burke–Ernzerhof approximation with the semiempirical Van der Waals correction (PBE+VDW) is suitable to describe the exchange–correlation energy functional

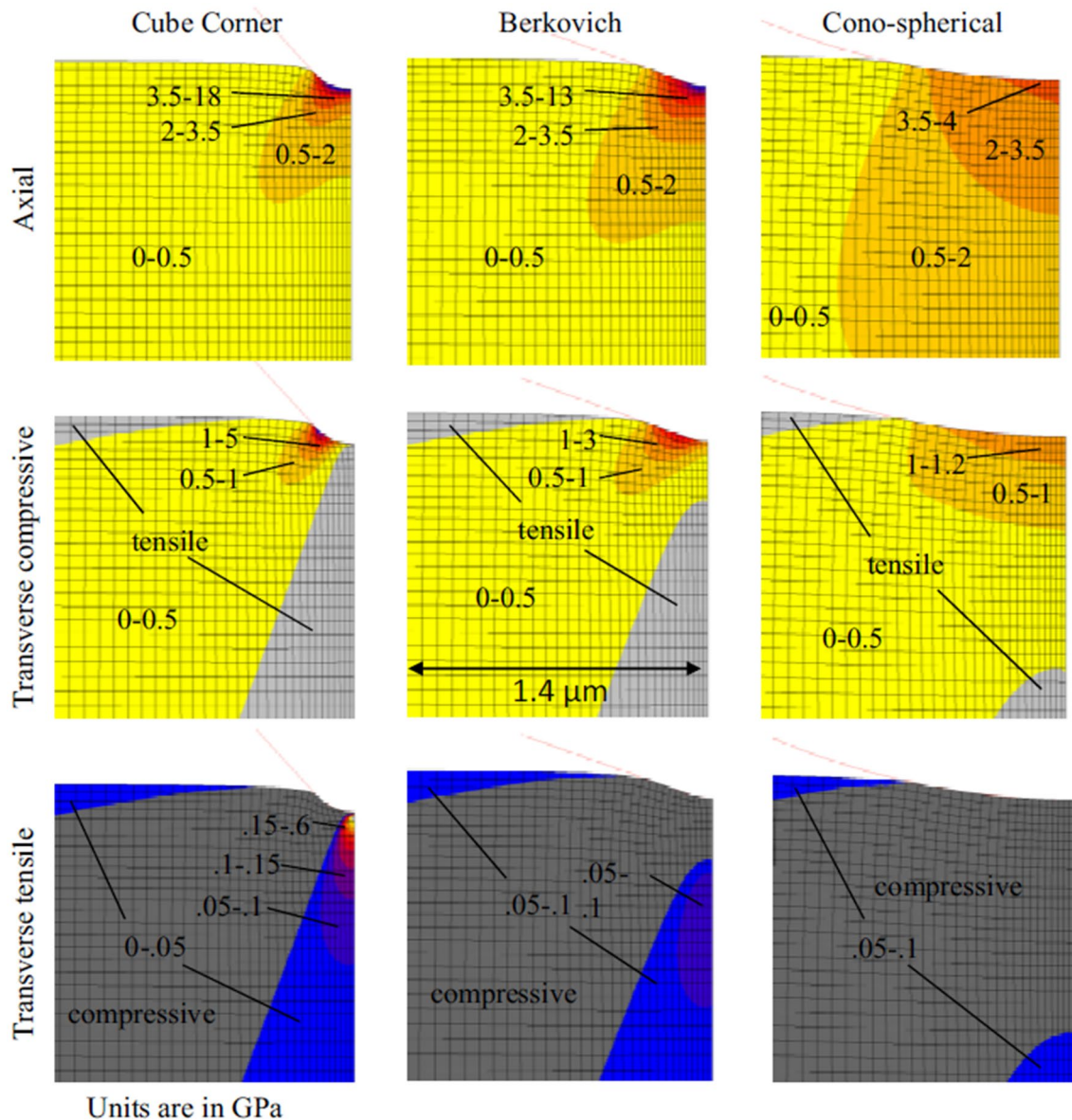


Fig. 7 Stress field for three different tip geometries obtained by means of FEM simulations. The simulation refers to an indentation performed in the plane of isotropy. The first, second, and third rows

show the axial stress (in the direction of indentation), the transverse compressive stress, and the transverse tensile stress, respectively [38]

of Bi_2Te_3 and leads to the correct estimation of the material elastic mechanical properties by DFT simulations. An example on the implementation of the Delafargue and Ulm's model for the characterization of transversely isotropic pyrolytic carbon is also provided. A discrepancy between experimental and theoretical results in the direction parallel to the plane of isotropy is observed and ascribed to a nanobuckling phenomenon. This phenomenon is more evident when a cube corner indenter is used, as demonstrated by FEM simulations. Although the Delafargue and Ulm's model does not take into

consideration the fully elastic deformation of pyrolytic carbon during indentation, good agreement between experimental and theoretical results is observed in direction perpendicular to the isotropy plane.

The contents proposed in this paper represent a useful tool toward the choice of a suitable model for the evaluation of the elastic properties of anisotropic materials at micro- and nano-scale by depth-sensing indentation technique.

Compliance with ethical standards

Conflict of interest The author declares that they have no conflict of interest.

References

- Mohs F (1822) Grundriss der Mineralogie. I. Theil. Terminologie, Systematik, Nomenklatur, Charakteristik
- Fischer-Cripps AC (ed) (2011) Nanoindentation testing. In: Nanoindentation. Springer, New York, pp 21–37
- Tabor D (1948) A simple theory of static and dynamic hardness. Proc R Soc Lond A 192(1029):247–274
- Stilwell N, Tabor D (1961) Elastic recovery of conical indentations. Proc Phys Soc 78(2):169
- Doerner MF, Nix WD (1986) A method for interpreting the data from depth-sensing indentation instruments. J Mater Res 1(4):601–609
- Pharr G, Oliver W, Brotzen F (1992) On the generality of the relationship among contact stiffness, contact area, and elastic modulus during indentation. J Mater Res 7(3):613–617
- Oliver WC, Pharr GM (1992) An improved technique for determining hardness and elastic modulus using load and displacement sensing indentation experiments. J Mater Res 7(6):1564–1583
- Lekhnitskii SG (1981) Theory of elasticity of an anisotropic body. Mir Publishers, Moscow
- Ting T (1996) Anisotropic elasticity. Oxford University Press, Oxford
- Vlassak JJ, Nix W (1993) Indentation modulus of elastically anisotropic half spaces. Philos Mag A 67(5):1045–1056
- Vlassak J, Ciavarella M, Barber J, Wang X (2003) The indentation modulus of elastically anisotropic materials for indenters of arbitrary shape. J Mech Phys Solids 51(9):1701–1721
- Barnett D, Lothe J (1975) Line force loadings on anisotropic half-spaces and wedges. Phys Nor 8(1):13–22
- Argatov I, Mishuris G (eds) (2018) Indentation of an anisotropic elastic half-space. In: Indentation testing of biological materials. Springer, Berlin, pp 323–371
- Delafargue A, Ulm F-J (2004) Explicit approximations of the indentation modulus of elastically orthotropic solids for conical indenters. Int J Solids Struct 41(26):7351–7360
- Lamuta C, Campi D, Cupolillo A, Aliev Z, Babanly M, Chulkov E et al (2016) Mechanical properties of Bi_2Te_3 topological insulator investigated by density functional theory and nanoindentation. Scr Mater 121:50–55
- Wang C, Potter AC, Senthil T (2014) Classification of interacting electronic topological insulators in three dimensions. Science 343(6171):629–631. <https://doi.org/10.1126/science.1243326>
- Caballero-Calero O, Martín-González M (2016) Thermoelectric nanowires: a brief prospective. Scr Mater 111:54–57. <https://doi.org/10.1016/j.scriptamat.2015.04.020>
- Jacimovic J, Mettan X, Pisoni A, Gaal R, Katrych S, Demko L et al (2014) Enhanced low-temperature thermoelectrical properties of BiTeCl grown by topotactic method. Scr Mater 76:69–72. <https://doi.org/10.1016/j.scriptamat.2013.12.017>
- Peng H, Dang W, Cao J, Chen Y, Wu D, Zheng W et al (2012) Topological insulator nanostructures for near-infrared transparent flexible electrodes. Nat Chem 4(4):281–286
- Nechaev IA, Aguilera I, De Renzi V, di Bona A, Lodi Rizzini A, Mio AM et al (2015) Quasiparticle spectrum and plasmonic excitations in the topological insulator Sb_2Te_3 . Phys Rev B 91(24):245123
- Vobornik I, Manju U, Fujii J, Borgatti F, Torelli P, Krizmancic D et al (2011) Magnetic proximity effect as a pathway to spintronic applications of topological insulators. Nano Lett 11(10):4079–4082
- Nayak C, Simon SH, Stern A, Freedman M, Das Sarma S (2008) Non-Abelian anyons and topological quantum computation. Rev Mod Phys 80(3):1083–1159
- Li D, Qin XY, Dou YC, Li XY, Sun RR, Wang QQ et al (2012) Thermoelectric properties of hydrothermally synthesized $\text{Bi}_2\text{Te}_{3-x}\text{Se}_x$ nanocrystals. Scr Mater 67(2):161–164. <https://doi.org/10.1016/j.scriptamat.2012.04.005>
- Liu Y, Zhou M, He J (2016) Towards higher thermoelectric performance of Bi_2Te_3 via defect engineering. Scr Mater 111:39–43. <https://doi.org/10.1016/j.scriptamat.2015.06.031>
- Zhang JL, Zhang SJ, Weng HM, Zhang W, Yang LX, Liu QQ et al (2011) Pressure-induced superconductivity in topological parent compound Bi_2Te_3 . Proc Natl Acad Sci USA 108(1):24–28. <https://doi.org/10.1073/pnas.1014085108>
- Yuan H, Liu H, Shimotani H, Guo H, Chen M, Xue Q et al (2011) Liquid-gated ambipolar transport in ultrathin films of a topological insulator Bi_2Te_3 . Nano Lett 11(7):2601–2605
- Lamuta C, Cupolillo A, Politano A, Aliev ZS, Babanly MB, Chulkov EV et al (2016) Indentation fracture toughness of single-crystal Bi_2Te_3 topological insulators. Nano Res 9(4):1032–1042
- Lamuta C, Cupolillo A, Politano A, Aliev ZS, Babanly MB, Chulkov EV et al (2016) Nanoindentation of single-crystal Bi_2Te_3 topological insulators grown with the Bridgman–Stockbarger method. Phys Status Solidi (b) 253(6):1082–1086
- Politano A, Lamuta C, Chiarello G (2017) Cutting a Gordian Knot: dispersion of plasmonic modes in Bi_2Se_3 topological insulator. Appl Phys Lett 110(21):211601
- Giannozzi P, Baroni S, Bonini N, Calandra M, Car R, Cavazzoni C et al (2009) QUANTUM ESPRESSO: a modular and open-source software project for quantum simulations of materials. J Phys Condens Matter 21(39):395502
- Perdew JP, Zunger A (1981) Self-interaction correction to density-functional approximations for many-electron systems. Phys Rev B 23(10):5048–5079
- Perdew JP, Burke K, Ernzerhof M (1996) Generalized gradient approximation made simple. Phys Rev Lett 77(18):3865–3868
- Grimme S (2006) Semiempirical GGA-type density functional constructed with a long-range dispersion correction. J Comput Chem 27(15):1787–1799. <https://doi.org/10.1002/jcc.20495>
- Monkhorst HJ, Pack JD (1976) Special points for Brillouin-zone integrations. Phys Rev B. 13(12):5188–5192
- Jochym PT, Parlinski K, Sternik M (1999) TiC lattice dynamics from ab initio calculations. Eur Phys J B 10(1):9–13. <https://doi.org/10.1007/s100510050823>
- Jochym PT, Parlinski K (2000) Ab initio lattice dynamics and elastic constants of ZrC. Eur Phys J B 15(2):265–268. <https://doi.org/10.1007/s100510051124>
- Li X, Bhushan B (2002) A review of nanoindentation continuous stiffness measurement technique and its applications. Mater Charact 48(1):11–36
- Gross T, Timoshchuk N, Tsukrov I, Piat R, Reznik B (2013) On the ability of nanoindentation to measure anisotropic elastic constants of pyrolytic carbon. ZAMM J Appl Math Mech 93(5):301–312
- Gross T, Timoshchuk N, Tsukrov I, Reznik B (2013) Unique nanoindentation damage for highly textured pyrolytic carbon. Carbon 60:273–279
- Jäger A, Bader T, Hofstetter K, Eberhardsteiner J (2011) The relation between indentation modulus, microfibril angle, and elastic properties of wood cell walls. Compos A Appl Sci Manuf 42(6):677–685

41. Jäger A, Hofstetter K, Buksnowitz C, Gindl-Altmutter W, Konnerth J (2011) Identification of stiffness tensor components of wood cell walls by means of nanoindentation. *Compos A Appl Sci Manuf* 42(12):2101–2109
42. Chen Q, Gao F, Csanádi T, Xu J, Fu M, Wang M et al (2018) Investigation of anisotropic mechanical properties of textured $\text{KSr}_2\text{Nb}_5\text{O}_{15}$ ceramics via ab initio calculation and nanoindentation. *J Am Ceram Soc* 101(11):5138–5150
43. Csanádi T, Németh D, Dusza J, Lenčes Z, Šajgalik P (2016) Nanoindentation induced deformation anisotropy in $\beta\text{-Si}_3\text{N}_4$ ceramic crystals. *J Eur Ceram Soc* 36(12):3059–3066
44. Jakob A, Müller M, Rauschenbach B, Mayr S (2012) Nanoscale mechanical surface properties of single crystalline martensitic Ni–Mn–Ga ferromagnetic shape memory alloys. *New J Phys* 14(3):033029
45. Yang R, Zaheri A, Gao W, Hayashi C, Espinosa HD (2017) AFM identification of beetle exocuticle: bouligand structure and nanofiber anisotropic elastic properties. *Adv Func Mater* 27(6):1603993
46. De Pauw V, Reznik B, Kalhöfer S, Gerthsen D, Hu Z, Hüttinger K (2003) Texture and nanostructure of pyrocarbon layers deposited on planar substrates in a hot-wall reactor. *Carbon* 41(1):71–77
47. Bourrat X, Trouvat B, Limousin G, Vignoles G, Doux F (2000) Pyrocarbon anisotropy as measured by electron diffraction and polarized light. *J Mater Res* 15(1):92–101
48. Gebert J-M, Reznik B, Piat R, Viering B, Weidenmann K, Wanner A et al (2010) Elastic constants of high-texture pyrolytic carbon measured by ultrasound phase spectroscopy. *Carbon* 48(12):3647–3650
49. Gross TS, Nguyen K, Buck M, Timoshchuk N, Tsukrov II, Reznik B et al (2011) Tension–compression anisotropy of in-plane elastic modulus for pyrolytic carbon. *Carbon* 49(6):2145–2147
50. Loidl D, Paris O, Burghammer M, Riekel C, Peterlik H (2005) Direct observation of nanocrystallite buckling in carbon fibers under bending load. *Phys Rev Lett* 95(22):225501
51. Sneddon IN (1965) The relation between load and penetration in the axisymmetric Boussinesq problem for a punch of arbitrary profile. *Int J Eng Sci* 3(1):47–57
52. Diss P, Lamon J, Carpentier L, Loubet J, Kapsa P (2002) Sharp indentation behavior of carbon/carbon composites and varieties of carbon. *Carbon* 40(14):2567–2579
53. Ozcan S, Tezcan J, Filip P (2009) Microstructure and elastic properties of individual components of C/C composites. *Carbon* 47(15):3403–3414
54. Carnelli D, Lucchini R, Ponzoni M, Contro R, Vena P (2011) Nanoindentation testing and finite element simulations of cortical bone allowing for anisotropic elastic and inelastic mechanical response. *J Biomech* 44(10):1852–1858
55. Ulm F-J, Abousleiman Y (2006) The nanogranular nature of shale. *Acta Geotech* 1(2):77–88
56. Ortega JA, Ulm F-J, Abousleiman Y (2007) The effect of the nanogranular nature of shale on their poroelastic behavior. *Acta Geotech* 2(3):155–182
57. Ebrahimi D, Whittle AJ, Pellenq RJ-M (2014) Mesoscale properties of clay aggregates from potential of mean force representation of interactions between nanoplatelets. *J Chem Phys* 140(15):154309
58. Ebrahimi D, Pellenq RJ-M, Whittle AJ (2012) Nanoscale elastic properties of montmorillonite upon water adsorption. *Langmuir* 28(49):16855–16863
59. Guicciardi S, Melandri C, Monteverde FT (2010) Characterization of pop-in phenomena and indentation modulus in a polycrystalline ZrB₂ ceramic. *J Eur Ceram Soc* 30(4):1027–1034
60. Jauffrès D, Yacou C, Verdier M, Dendievel R, Ayrat A (2011) Mechanical properties of hierarchical porous silica thin films: experimental characterization by nanoindentation and Finite Element modeling. *Microporous Mesoporous Mater* 140(1–3):120–129
61. Delobelle P, Fribourg-Blanc E, Remiens D (2006) Mechanical properties determined by nanoindentation tests of [Pb (Zr, Ti) O₃] and [Pb (Mg_{1/3}Nb_{2/3})_{1-x}Ti_xO₃] sputtered thin films. *Thin Solid Films* 515(4):1385–1393
62. Andrei A, Krupa K, Jozwik M, Delobelle P, Hirsinger L, Gorecki C et al (2008) AlN as an actuation material for MEMS applications: the case of AlN driven multilayered cantilevers. *Sens Actuators A* 141(2):565–576
63. Delobelle P, Wang G, Fribourg-Blanc E, Remiens D (2007) Indentation modulus and hardness of Pb (Zr, Ti) O₃ sol–gel films deposited on Pt and LaNiO₃ electrodes: an estimation of the CijD compliances. *J Eur Ceram Soc* 27(1):223–230

Publisher's Note Springer Nature remains neutral with regard to jurisdictional claims in published maps and institutional affiliations.